

Nucleate Pool Boiling CFD simulation

Yanis Mondet

January 3, 2025

Abstract

This report presents the development of a CFD simulation for modelling nucleate pool boiling on OpenFOAM. It takes place in the course Numerical project at Grenoble INP - ENSE3.

1 Introduction

Boiling phenomena occur in a wide range of engineering applications, such as vapor generators in nuclear power plants. Understanding boiling is crucial for optimizing these systems. However, boiling heat transfer is highly complex and no full comprehensive theory currently describes boiling across all conditions and applications. Boiling heat transfer can be studied at different length scales, from individual bubble dynamics to interaction between water and vapor phases.

One approach for simulating boiling is Computational Fluid Dynamics (CFD) simulation. In this project, boiling is studied through numerical simulation at the scale of a single bubble. The open-source software OpenFOAM version V2106 was used, employing and modifying a solver developed in [1] and detailed in [2] by Municchi and Magnini.

This report first presents an overview of boiling modelling and a description of the numerical model used for this simulation. Then, the bubble detachment studied by Georgoulas et al. [3] is reproduced and the influence of various parameters is studied and their effects are compared on the boiling process.

2 Boiling modelling

2.1 An overview of boiling

Boiling, a heat transfer mechanism that involves phase change, occurs when a liquid interacts with a heated surface or interface, leading to the evaporation of the liquid. Pool boiling is a specific case where there is no imposed fluid flux, the initial state of the liquid is at rest. This process includes several regimes: single-phase regime, nucleate boiling, transition boiling, and film boiling. Each regime is characterized by different heat transfer mechanisms, as described in the boiling curve Figure 1.

2.1.1 Nucleate Boiling

In the nucleate boiling regime, vapor bubbles form at discrete sites on the heated surface. Bubble dynamics, including their formation, growth, and detachment, is critical for efficient heat transfer. Heat transfer is enhanced by both latent heat and localized convection as bubbles disrupt the thermal boundary layer.

The nucleate boiling regime begins with the formation of bubbles at low heat flux (Figure 2a). Initially, detached bubbles condense as they rise in the liquid at saturation. As the heat flux increases, the production of vapor increases as well, provoking bubble coalescence parallel or perpendicular to the surface (Figure 2b). The proportion of vapor near the surface increases until the critical point is reached.

Homogeneous and heterogeneous Nucleation Homogeneous nucleation occurs when vapour bubbles spontaneously form within a superheated liquid due to thermal fluctuations, independent of surfaces or impurities. A bubble becomes stable if its radius exceeds the critical radius r^* , which

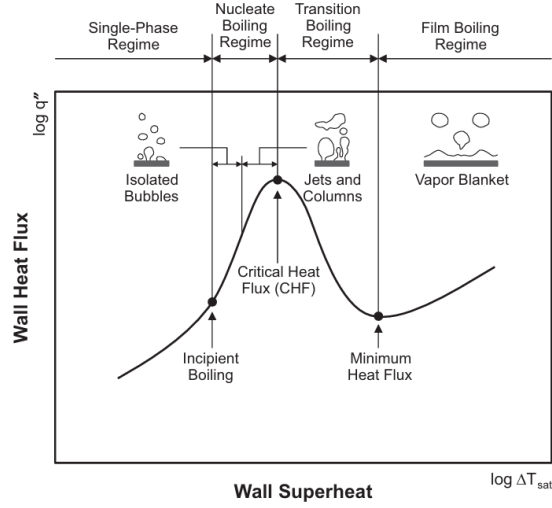


Figure 1: Boiling curve [4]

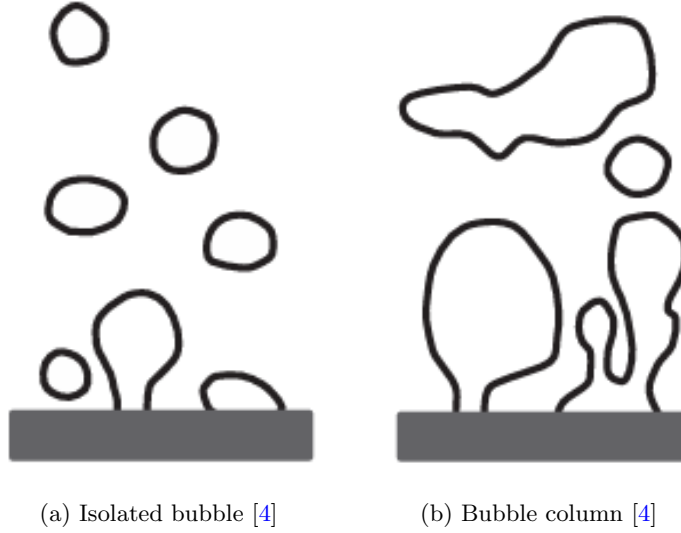


Figure 2: Comparison of isolated bubble and bubble column during pool boiling.

depends on the surface tension of the liquid and the pressure difference. The process involves overcoming a significant energy barrier, as smaller bubbles ($r < r^*$) collapse, while larger bubbles ($r \geq r^*$) grow. Because of the high-energy requirement, homogeneous nucleation is rare and typically requires substantial superheating of the liquid.

Heterogeneous nucleation, in contrast, occurs at specific sites on solid surfaces or impurities, where the energy barrier is lower. While the critical radius r^* remains the same as in homogeneous nucleation, the energy barrier is reduced by a shape factor dependent on the contact angle θ between the bubble and the surface. This modification makes bubble formation much easier in heterogeneous nucleation, which is far more common in real-world applications due to the reduced superheating requirement.

Bubble Growth and Detachment Once a vapor bubble forms and surpasses the critical radius r^* , it grows and eventually detaches from the heated surface. The growth process occurs in two primary stages:

1. **Inertial Growth:** The initial stage, dominated by liquid inertia, involves rapid bubble expansion due to the pressure difference between the vapor inside the bubble and the surrounding liquid.
2. **Thermal Growth:** At later stages, bubble growth is governed by heat transfer, with the rate

limited by heat conduction through the liquid to the bubble interface.

Bubble detachment occurs when the buoyancy force F_b exceeds the surface tension force F_σ , satisfying the condition:

$$F_b = F_\sigma,$$

There are cycles of bubble growth and detachment. After detachment, the nucleation site becomes inactive for a defined time as it is cooled by liquid at the saturation temperature. This process is crucial for enhancing heat transfer during nucleate boiling as the periodic detachment of bubbles refreshes the liquid near the heated surface.

2.1.2 Critical Heat Flux (CHF)

As observed on the boiling curve 1, when we increase the wall heat flux from nucleate boiling regime, the wall superheat progressively increases until it reaches a maximum named critical heat flux. It represents the maximum heat flux a surface can sustain before the liquid's contact with the surface is disrupted by vapor. Beyond this point, vapor blankets the surface, significantly reducing heat transfer due to the low thermal conductivity of vapor. The CHF marks the peak of heat transfer efficiency before transitioning to film boiling. After the CHF, for a constant heat flux the wall superheat keep improving until reaching the film boiling regime.

2.1.3 Transition Boiling Regime

In the film boiling regime, the heated surface is fully covered by a vapor film. Periodically, large bubbles detached from the vapor blanket. Heat transfer occurs primarily through conduction across the vapor film to vaporize the liquid at the interface and at high heat fluxes, radiative heat transfer also plays a significant role as surface temperatures can reach several hundred degrees Celsius.

Then, if the heat flux is decreased, the vapor film can remain stable for fluxes below the critical heat flux. This remains stable until the Leidenfrost point, which is the minimum heat flux where we still get a stable film. If the flux decreases further, the regime destabilizes, transitioning to nucleate boiling.

2.2 Basic knowledge about multiphase flow simulation

2.2.1 Volume of fluid model

Since in our case we don't need to follow the bubble we are going to use an Eulerian model. There are two possible model: VOF method or the Euler-Euler model. Firstly, we are going to use the VOF method in order to simulate the flow.

The **Volume of Fluid (VOF)** model is used to track and locate the interface between two immiscible fluids, such as liquid and vapor, in multiphase flow simulations. The VOF model introduces a **volume fraction field** α to represent the presence of each fluid in a computational cell.

The volume fraction α represents the fraction of the cell occupied by the liquid phase:

$$\alpha = \begin{cases} 1, & \text{cell fully liquid} \\ 0, & \text{cell fully vapor} \\ 0 < \alpha < 1, & \text{interface region (mixed cell)} \end{cases}$$

The interface is represented by cells where $0 < \alpha < 1$. In these mixed cells, the interface can be approximated using techniques like the Piecewise Linear Interface Calculation (PLIC), which provides an accurate representation of the boundary between the phases.

In cells containing the interface, the fluid properties such as density ρ and viscosity μ are computed as weighted averages based on α :

$$\rho = \alpha\rho_l + (1 - \alpha)\rho_v, \tag{1}$$

$$\mu = \alpha\mu_l + (1 - \alpha)\mu_v, \tag{2}$$

where ρ_l and μ_l are the properties of the liquid phase, and ρ_v and μ_v are the properties of the vapor phase.

2.2.2 Volume fraction equation

The volume fraction equation is:

$$\frac{\partial \alpha}{\partial t} + \nabla \cdot (\alpha \mathbf{u}) = -\frac{1}{\rho_1} m_i'' \nabla \alpha$$

where:

- α : volume fraction of liquid phase (ranges from 0 for vapor to 1 for liquid),
- \mathbf{u} : velocity vector of the flow,
- m_i'' : phase change rate per unit area (interface mass flux, measured in kg/m²/s),
- ρ_1 : density of the liquid phase.

This equation describes how the volume fraction of the liquid phase changes due to advection and phase change at the interface.

2.2.3 Incompressibility Condition

The incompressibility condition is modified to account for phase change, incorporating densities of both phases:

$$\nabla \cdot \mathbf{u} = \frac{1}{\rho_2} - \frac{1}{\rho_1} m_i'' \nabla \alpha$$

where ρ_2 is the density of the vapor phase.

This ensures that the divergence of velocity considers the density difference due to phase transition between liquid and vapor.

2.2.4 Energy Equation

The energy conservation equation integrates conductive and convective heat transfer with latent heat effects at the phase boundary:

$$\frac{\partial(\rho c_p T)}{\partial t} + \nabla \cdot (\rho c_p \mathbf{u} T) = \nabla \cdot (\lambda \nabla T) - m_i'' h_{lv} \nabla \alpha$$

where:

- T : temperature,
- c_p : specific heat capacity,
- λ : thermal conductivity,
- h_{lv} : latent heat of vaporization.

This equation models the thermal behavior of the system, incorporating both the heat diffusion in the bulk phases and the heat required for phase change at the interface.

2.2.5 Momentum Conservation (Navier-Stokes Equation)

The momentum equation includes terms for pressure, viscosity, and surface tension at the interface:

$$\frac{\partial(\rho \mathbf{u})}{\partial t} + \nabla \cdot (\rho \mathbf{u} \mathbf{u}) = -\nabla p + \nabla \cdot \boldsymbol{\tau} + \mathbf{F}_\sigma$$

where:

- p : pressure,
- $\boldsymbol{\tau}$: viscous stress tensor,
- \mathbf{F}_σ : surface tension force.

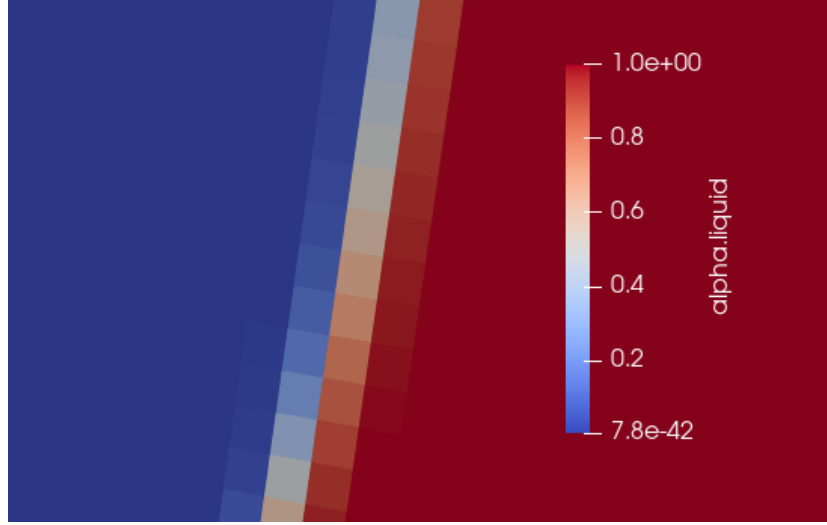


Figure 3: Interface of the bubble

2.2.6 VOF methods

Two main Volume of Fluid (VOF) methods have been developed the algebraic and geometric approaches. The main differences are explained using the review of Mulbah et al.[5]. In algebraic VOF (AVOF) methods, the volume fraction α is represented as a mathematical function, while in geometric VOF (GVOF) methods, α is represented explicitly through interface geometry.

Algebraic methods are relatively easier to implement and more computationally efficient. However, they often create numerical diffusion, require artificial compression schemes, and lose accuracy at high Courant numbers. These methods are generally less accurate compared to geometric methods but are preferred for cases where computational efficiency is a priority.

Geometric methods, on the other hand, offer accurate interface advection and are better suited for preserving sharp interfaces. They work well on unstructured meshes and are preferred for complex flow problems. However, their implementation is computationally intensive, especially in three-dimensional cases, as they require complex geometric operations and reconstructions.

Overall, AVOF methods are efficient for simpler applications, while GVOF methods are more accurate and reliable for challenging simulations involving detailed interface dynamics.

2.2.7 Interface Conditions

The **interface indicator function** I specifies the phase (liquid or vapor) at each point, defined as:

$$I(\mathbf{x}, t) = \begin{cases} 1, & \text{in liquid} \\ 0, & \text{in vapor} \end{cases}$$

The volume fraction α is then calculated by integrating I over a control volume V :

$$\alpha = \frac{1}{V} \int_V I(\mathbf{x}, t) dV$$

This function determines the local phase within the control volume and guides phase change calculations by indicating where α transitions.

We can see in Figure 3 that for a mesh with 1 micrometer cells, the interface is contained in only three cells. When, talking of a parameter at the interface for instance temperature, we talk about the temperature of the middle cell of the interface.

2.2.8 Surface tension force

For the surface tension force we use the Continuum Surface Force (CSF) model [6] given by:

$$\mathbf{F}_\sigma = 2 \frac{\rho}{\rho_l + \rho_v} \sigma \kappa \nabla \alpha$$

where: - σ : surface tension coefficient, - κ : interface curvature, - ρ : effective density based on the volume fraction, $\rho = \rho_2 + (\rho_1 - \rho_2)\alpha$.

The curvature κ of the surface is calculated using the formula:

$$\kappa = -\nabla \cdot \hat{n}, \quad (3)$$

where \hat{n} is the unit normal vector to the surface. The derivation of this formula can be found in the appendix for completeness.

$$n(x) = \nabla \alpha(x). \quad (4)$$

The unit normal vector is then obtained as:

$$\hat{n}(x) = \frac{\nabla \alpha(x)}{|\nabla \alpha(x)|}. \quad (5)$$

2.2.9 Phase Change with the Hardt and Wondra Model

The interfacial mass flux m_i'' is modeled according to Hardt and Wondra [7]:

$$m_i'' = \frac{h_i}{h_{lv}} (T_i - T_{sat}) \quad (6)$$

where:

- T_i is the temperature at the interface.
- T_{sat} is the saturation temperature at the interfacial pressure.
- h_i is the interfacial heat transfer coefficient given by:

$$h_i = \left(\frac{2\gamma}{2 - \gamma} \right) \rho_v h_{lv} \left(\frac{\bar{M}}{2\pi \bar{R}} \right)^{1/2} \left(\frac{p_v}{T_{sat}^3} \right)^{1/2} \quad (7)$$

- γ is an accommodation coefficient (typically between 0 and 1).
- \bar{M} is the molar mass.
- \bar{R} is the universal gas constant.
- p_v is the vapor pressure at the interface.

Together, these equations govern the conservation of phase fraction, momentum, and energy in the "boilingFoam" solver, allowing it to accurately simulate phase change dynamics such as boiling and condensation by resolving heat transfer, interface movement, and density differences across phases.

3 Numerical model validation

To validate the solver, a test case included in the solver was tested and subsequently adapted to different configurations, with the results compared to analytical solutions.

3.1 Bubble Growth Theory

Bubble growth is a basic test case used to validate multiphase solver, Scriven [8] developed a numerical solution for bubble growth in a saturated liquid. The bubble radius $R(t)$ follows the law:

$$R(t) = 2\beta\sqrt{Dt}, \quad (8)$$

where β is given by:

$$\beta = J_a\sqrt{\frac{3}{\pi}}, \quad (9)$$

and the Jacob number J_a is defined as:

$$J_a = \frac{(T_\infty - T_{\text{sat}})\rho_l c_{p,l}}{\rho_v h_{l,v}}. \quad (10)$$

This boundary layer, derived from thermal diffusion theory (without additional heat sources), is defined by the following equation:

$$\delta = 2\sqrt{Dt}, \quad (11)$$

where D is the thermal diffusivity and t is the time required for the bubble to reach its current size. Using this formula in combination with the Scriven radius equation, we obtain:

$$\delta = \frac{R(t)}{\beta}, \quad (12)$$

where R is the bubble radius and β is a growth factor.

3.2 Test Cases

3.2.1 Definition of General Parameters

After testing the solver with the included test cases, we modified one of them to simulate bubble growth in saturated water with a temperature difference (ΔT) of 5°C. A 2D axisymmetric geometric approach is employed due to limited computational power. A bubble with an initial diameter of 100 μm is expected to grow to 500 μm within 2 ms. The initial conditions consist of a vapor bubble at 373.15 K surrounded by liquid at 378.15 K. To ensure both convergence and physical accuracy, the initial thermal boundary layer δ is added as an initial condition.

The boundary conditions (BC) for this simulation are as follows:

- **Axis (Left Boundary):** Symmetry boundary condition, implying no flux across this boundary. This reduces the computation to half of the domain.
- **Top Boundary:**
 - Fixed value for pressure (P)
 - Zero gradient for α (volume fraction), T (temperature), and U (velocity)
- **Right Boundary:**
 - Fixed value for pressure (P)
 - Zero gradient for α , T , and U
- **Bottom Boundary:** Symmetry boundary condition

To validate the solver while keeping computation times manageable, we limit the simulation to the first 0.4 ms of growth. This allows for a smaller domain and reduces the overall calculation time. We conduct a mesh convergence analysis using a structured square mesh, as shown in the Figure 4. The domain size is set to $L = 0.5$ mm, ensuring that the bubble remains smaller than half the domain size throughout the simulation.

Property	Unit	Liquid	Vapour
Density, ρ	kg m^{-3}	958	0.597
Specific heat capacity, c_p	$\text{J kg}^{-1} \text{K}^{-1}$	4220	2030
Thermal conductivity, k	$\text{W m}^{-1} \text{K}^{-1}$	0.679	0.025
Dynamic viscosity, μ	Pa s	2.77×10^{-4}	1.30×10^{-5}
Heat of vaporization, h_{lv}	J kg^{-1}	2,257,000	
Surface tension, σ	N m^{-1}	0.059	
Saturation temperature, T_{sat}	K	373.15	
Pressure, P	bar	1.013	
Growth constant, β	-	14.59	
Initial thermal layer thickness, δ_{therm}	m	7.00×10^{-6}	
Thermal diffusivity, D	$\text{m}^2 \text{s}^{-1}$	1.68×10^{-7}	
Superheat, ΔT	K	5	
Additional Simulation Parameters			
Initial bubble diameter	μm	100	
Target bubble diameter	μm	500	
Simulation time	ms	0.4	
Domain size, L	mm	0.5	
Temperature inside bubble	K	373.15	
Temperature in liquid	K	378.15	
Courant number (CFL)	-	0.2	
Mesh size, Δ_x	μm	1–2	

Table 1: Summary of Parameters for Bubble Growth Simulation

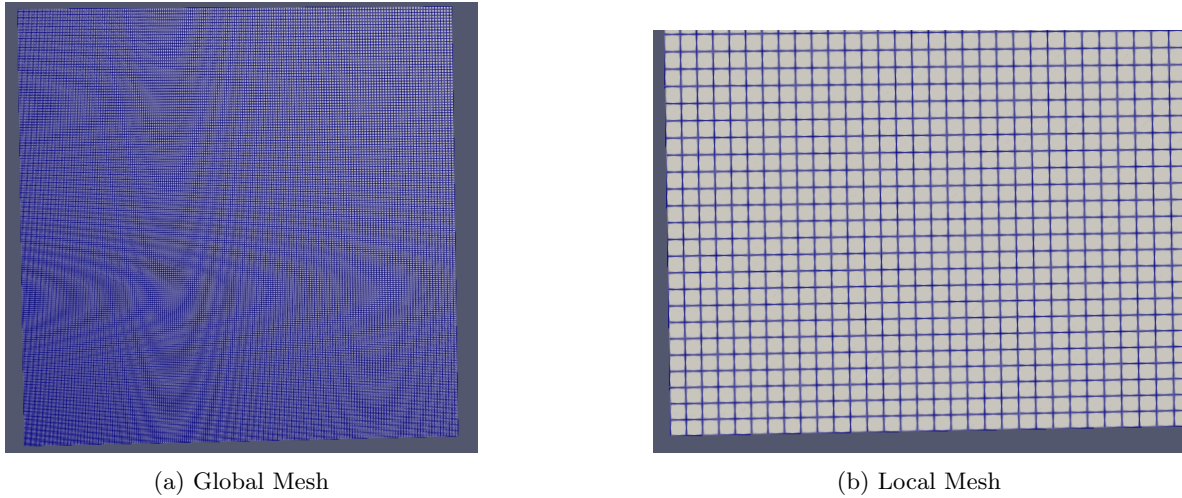


Figure 4: Comparison of Global and Local Meshes

A crucial parameter in CFD simulations is the Courant–Friedrichs–Lewy (CFL) number. After testing various Courant numbers, we observed that a CFL of 0.02 provides high accuracy but results in very long computation times. Conversely, a CFL of 1 speeds up the calculation but leads to poor resolution, with deformations observed at the bubble boundary, as shown in the Figure 5.

Ultimately, a Courant number of 0.2 was chosen as a good balance between accuracy and computation time.

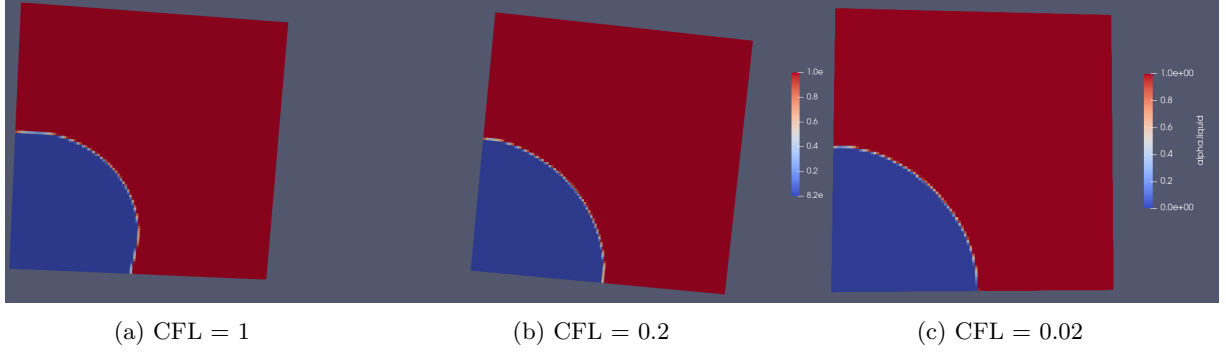


Figure 5: Comparison of CFL conditions at different settings.

Finally, I attempted to double the size of the initial boundary layer for a square mesh with cells of $2\ \mu\text{m}$, see 6. Doubling the initial thermal boundary layer thickness accelerates the computation time since the thermal gradient is smaller when the boundary layer (BL) larger. Initially, the larger BL appears to yield better results. However, this could be due to random variation and further investigation is required to confirm this observation. For the remainder of the study, we will keep using the thermal BL determined based on Scriven's theory.

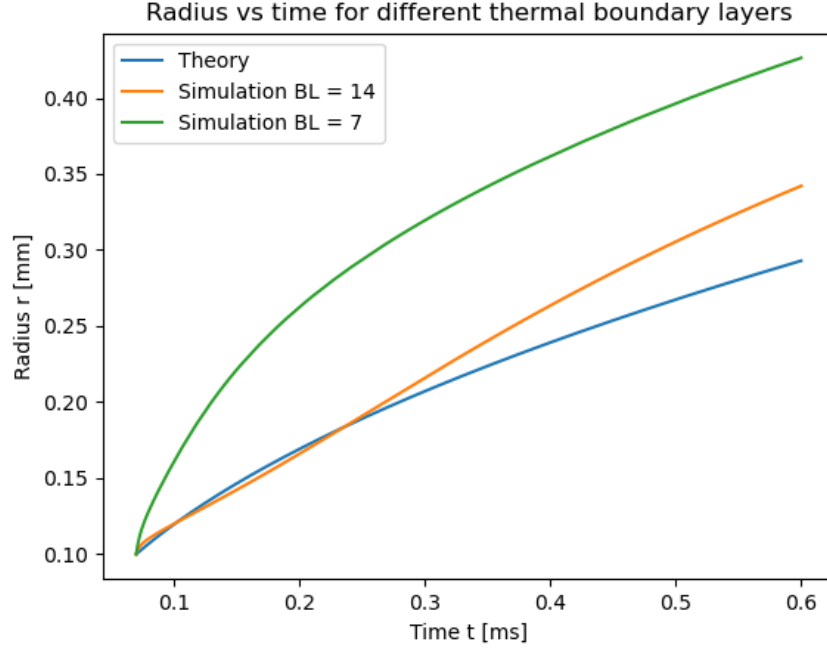


Figure 6: Initial BL impact on the results

3.2.2 Mesh convergence

Returning to the initial temperature difference (ΔT) of 5°C , we proceed with mesh convergence testing. For this test case we don't take into account gravity and surface tension. As seen in the Figure 4, a mesh size Δ_x of $1\ \mu\text{m}$, provides precise results but requires 5 hours to simulate just 0.4 ms of bubble growth. A $2\ \mu\text{m}$ mesh size, though less accurate, reduces the computation time to 45 minutes. A compromise between precision and efficiency has to be found according to what we want to study. Mesh cells of $1\ \mu\text{m}$ result in an error below 5%, whereas mesh cells of $2\ \mu\text{m}$ produce an error of approximately 30%.

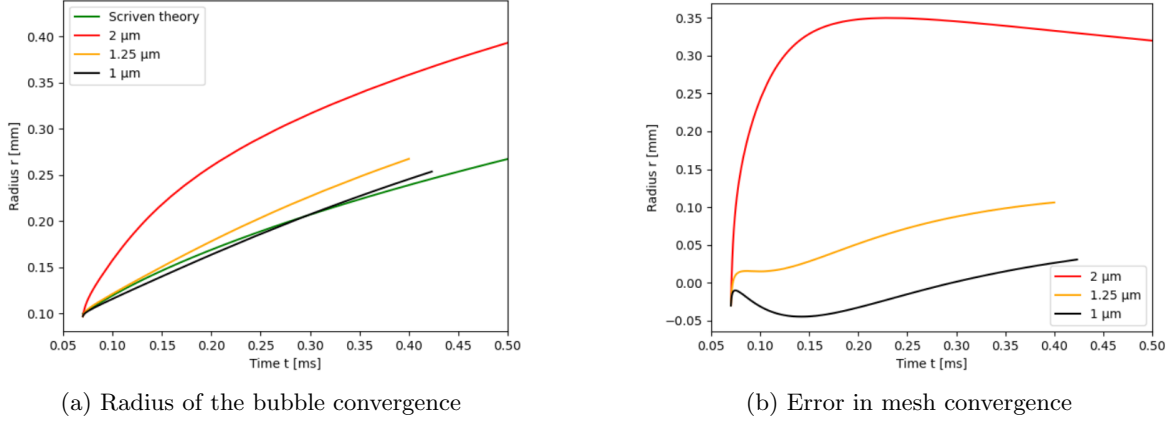


Figure 7: Comparison of mesh convergence for radius and errors.

3.2.3 VOF method and stability

As we observed, there are two primary methods to simulate the impact of surface tension. First, an algebraic VOF (Volume of Fluid) method was tested. However, this approach exhibited instability when incorporating the surface tension force. The source of the instability appears to originate near the axis, likely due to the small dimensions of the cells in the axisymmetric region. Specifically, to improve accuracy, an interface smoothing process is performed, during which terms are divided by the cell face area. In axisymmetric geometries, these areas can be exceedingly small, potentially leading to numerical errors.

Despite attempts to adjust various parameters, the instabilities could not be sufficiently mitigated. Therefore, we ultimately decided to test a geometric VOF method. Although this method also exhibited instabilities that caused unphysical phenomena near the axis (as illustrated in Figure 8), the overall results remained physically and numerically consistent. Consequently, the algebraic VOF MULES (Multidimensional Universal Limiter for Explicit Solution) scheme was selected for the remainder of the study.

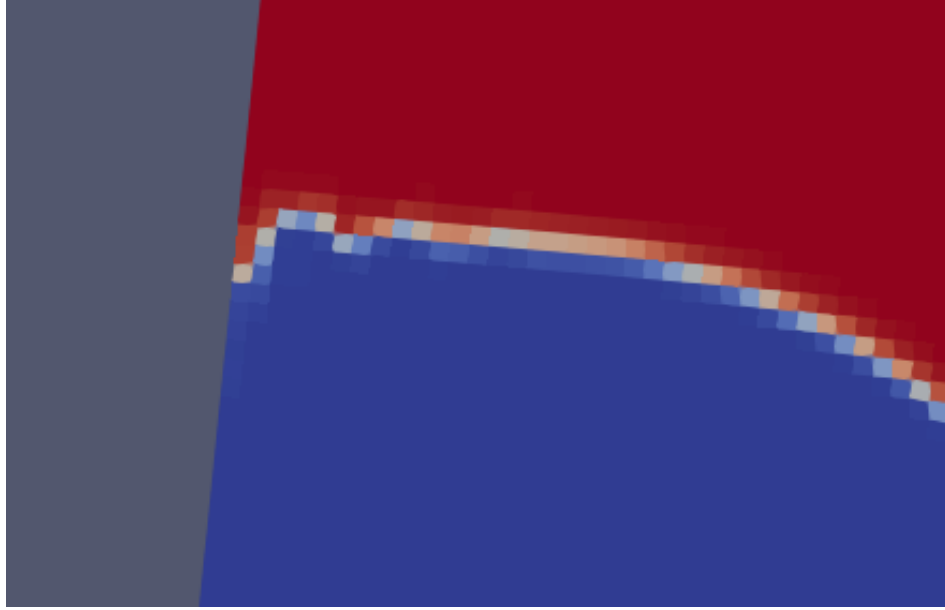


Figure 8: Instability at the interface near the axis

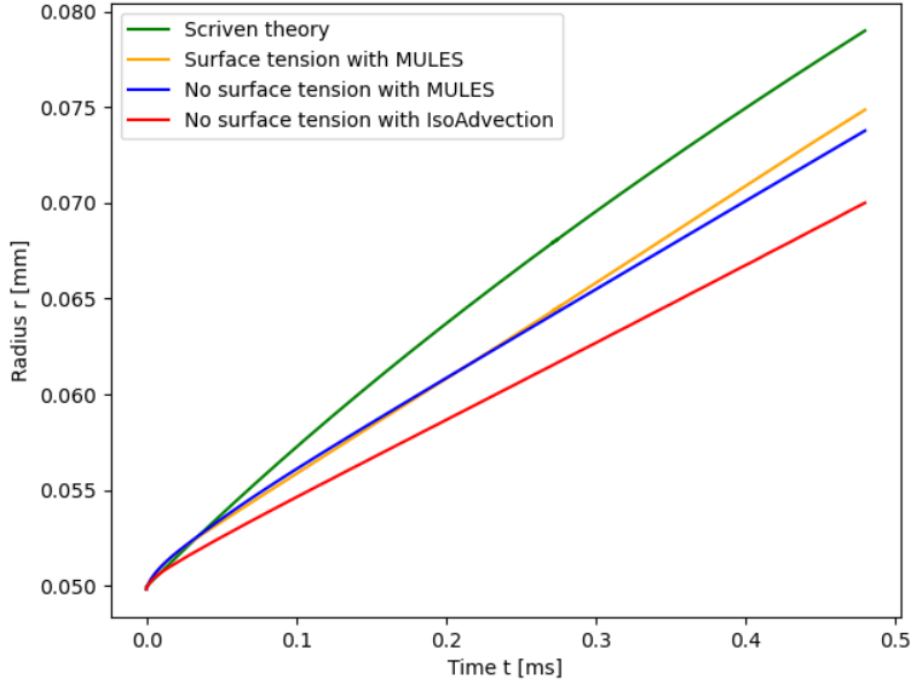


Figure 9: Comparison of various numericals VOF schemes

3.3 Study of bubble detachment

3.3.1 Setup for bubble detachment

With assurance that our solver provides acceptable results (see Figure 9), and after testing various hypotheses on the parameters to optimize computation time, this section focuses on the bubble detachment process in a pool boiling configuration for saturated R134a.

For this part, we take into account the impact of gravity with an intensity $g = 9.81 \text{ m/s}^2$ and the effect of surface tension.

The computational domain setup assumes the bottom and right faces are walls, while the top face is defined as an outlet. The domain parameters are summarized in Table 2.

Initially, a model is tested using the same parameters as shown in Figure 14. These parameters are detailed in Table ??.

Aspect	Details
Computational Domain	Axisymmetric, wedge-type geometry representing 5% of the 3D domain, uniform structured mesh, domain size: $0.2 \text{ mm} \times 0.1 \text{ mm}$.
Mesh Details	20,000 hexahedral cells, cell size: $1 \mu\text{m}$.
Boundary Conditions (Velocity)	No-slip velocity at solid walls; at outlet: zero gradient for outflow.
Boundary Conditions (Pressure)	Fixed flux pressure at solid walls; fixed-value pressure at outlet.
Boundary Conditions (Volume Fraction)	Zero-gradient at sidewall and outlet; contact angle of $\theta = 30^\circ$ at lower wall.
Boundary Conditions (Temperature)	Bottom wall: constant $T_w = 246.79 \text{ K}$; sidewall: zero-gradient; outlet: zero-gradient.

Table 2: Summary of computational domain, mesh, and boundary conditions.

As observed in the study by Georgoulas et al. (Figure 14), the temperature difference between the

wall and the fluid's saturation temperature has a significant impact on bubble detachment time and diameter.

The higher the wall temperature, the longer the detachment time and the larger the bubble diameter. Due to computational limitations, we chose a small temperature difference of 2.5K for our simulations with R134a. This choice allowed us to use a smaller computational domain and perform simulations over a shorter time frame.

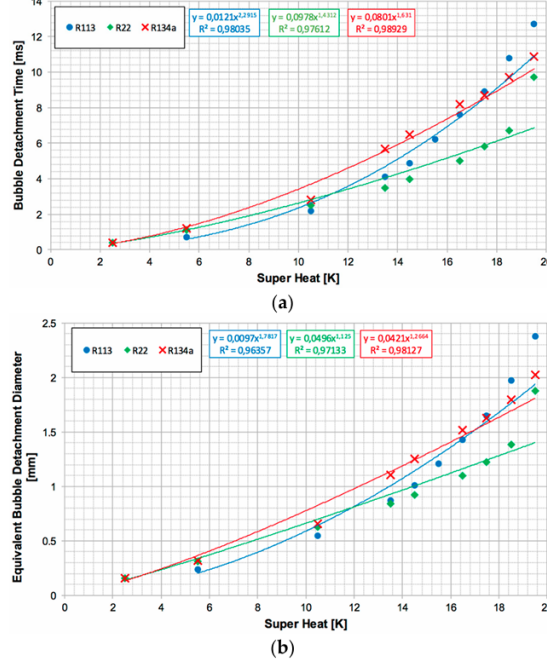


Figure 10: Impact of the wall superheat [3]

In this case, we use the same thermal boundary layer around the bubble as in the bubble growth analysis. Additionally, we introduce a thermal boundary layer at the heated wall to compare our results with those of Georgoulas et al. [3]. This thermal boundary layer, as illustrated in Figure 11, is assumed to have a thickness of 352 μm .

We model the temperature distribution within the boundary layer using an exponential profile, ensuring that the boundary layer thickness of 352 μm corresponds to 99% of the temperature variation between the wall temperature and the saturation temperature. The expression for the temperature profile is given as:

$$T(z) = 246.79 + (249.29 - 246.79) \cdot \exp\left(-\frac{4 \cdot z}{0.000352}\right)$$

The coefficient 4 was determined through multiple tests to ensure the boundary layer thickness matches the expected value.

3.3.2 Comparison of the results

From Figure 10, we observe that for a 2.5 K superheated wall, the expected bubble detachment diameter for R134a is approximately 150 μm , with a detachment time of around 0.4 ms.

With our solver, we get a bubble detachment time of 0.41 ms and a bubble detachment diameter of 152.6 μm . Considering the precision of our results, we achieve this with an uncertainty of about 10%, which arises from the interpretation of the diagram and the accuracy of our simulation. The bubble radius and diameter are defined as the radius and diameter of a perfectly spherical bubble with the same volume which can be found numerically with the void fraction.

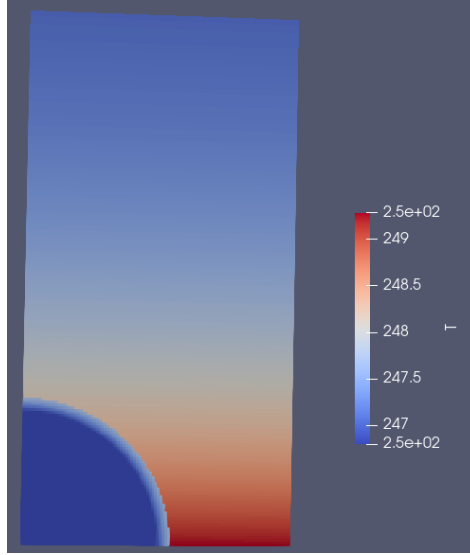


Figure 11: Wall thermal boundary layer

3.3.3 Impact of various parameters

Various parameters impact the bubble detachment, in this section we test the importance of the contact angle and the temperature of the wall.

Variation of Contact Angle: The contact angle significantly influences the dynamics of nucleate boiling. By varying the imposed contact angle in the simulation, we can observe changes in bubble growth rates and detachment radius. We can observe in the figure 13 that the higher the contact angle the larger the bubble detachment radius and time. We observe an important increase of the bubble detachment radius and time when passing from hydrophilic surface (low contact angle) to hydrophobic surface (high contact angle) at 45 degrees. The high increase found in our simulation is not exactly at 45 degrees but around 35 degrees. We do not do the calculation for higher contact angle because the bubble detachment time and radius are larger and then we need a bigger domain so the calculation time becomes too long.

Variation of Superheat Temperature: On the other hand, we try to impose various temperatures on the wall surface in order to evaluate the impact of the temperature on the bubble. We see in figure 14 that the higher the temperature difference between the wall surface and the bulk, the higher the detachment radius and time. These results are consistent with the study of [3] who did it for a larger range of temperatures and for different fluids.

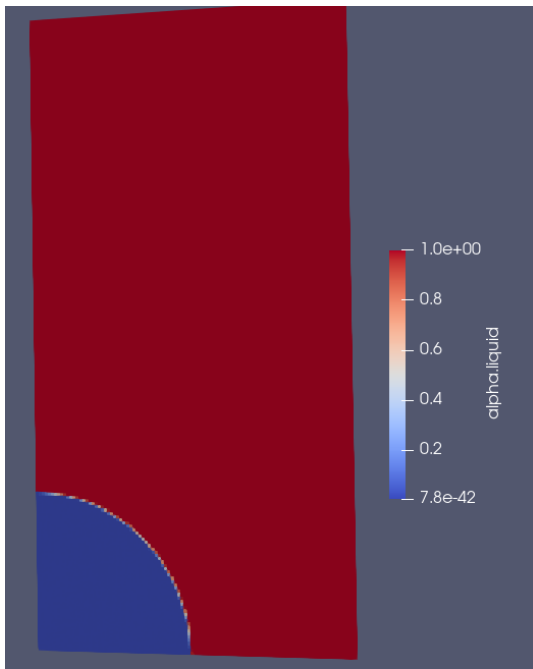
4 Conclusion

The simulation of nucleate pool boiling using the VOF method in OpenFOAM provided information on the dynamics of bubble growth and detachment. By improving and validating a numerical model against established theoretical and experimental data, we confirmed its ability to replicate key physical phenomena accurately within acceptable uncertainty levels.

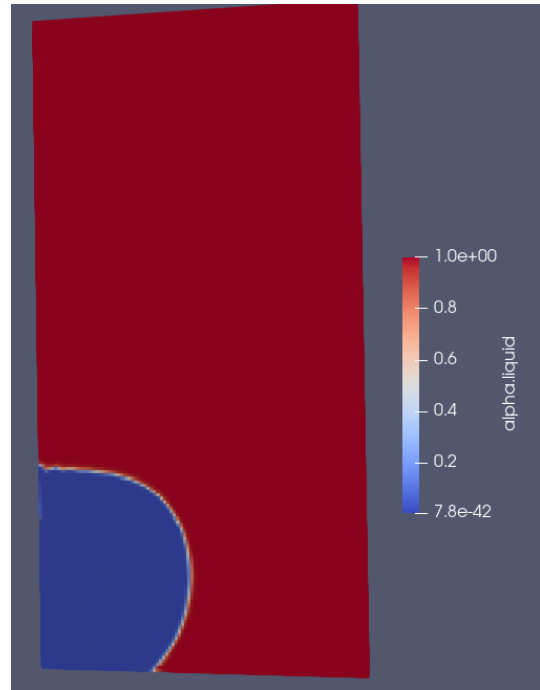
Challenges such as mesh convergence, stability near interfaces for axisymmetric simulation, and computational cost were encountered. To get more accurate results, it would be interesting to do the simulation with a 3D domain and with a fully converged mesh. Nevertheless, more powerful computational facilities are needed in that case.

The study highlighted the significant impact of surface characteristics, such as contact angle, and thermal parameters, such as wall superheat, on the boiling process. A higher contact angle led to larger detachment radius and prolonged detachment times, indicating the influence of surface hydrophobicity. Similarly, increased wall superheat resulted in accelerated bubble dynamics and enhanced heat transfer.

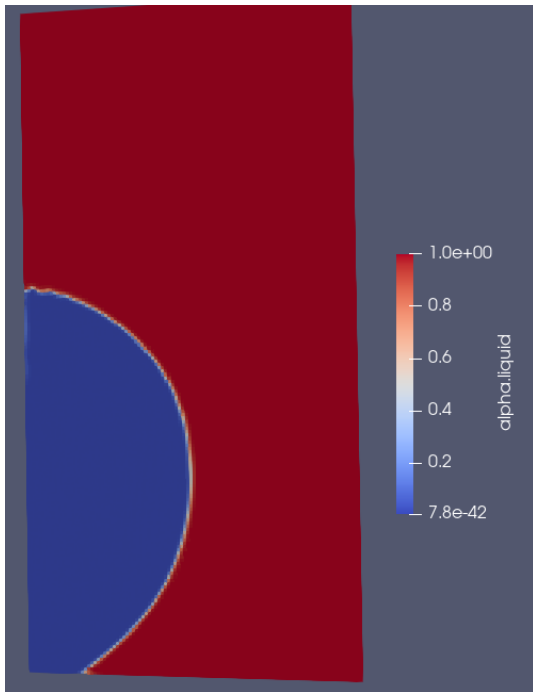
Incorporating a solid part in the domain as well as a heat source could be more realistic by taking into account the properties of the material used.



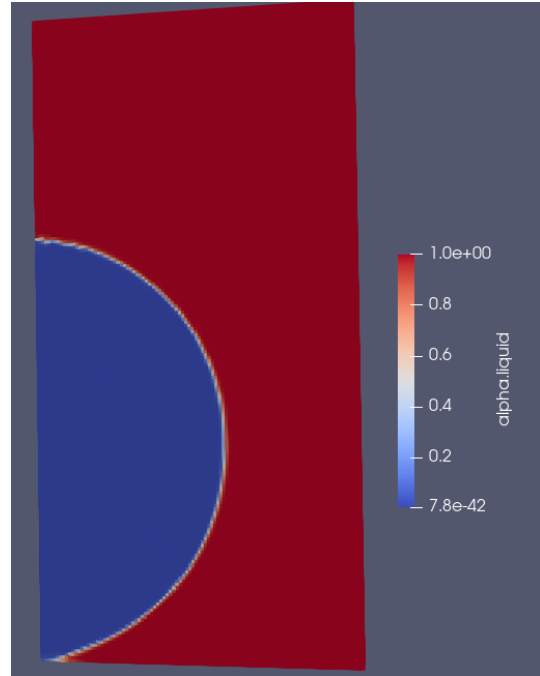
(a) $t = 0 \mu s$



(b) $t = 6 \mu s$



(c) $t = 20 \mu s$



(d) $t = 40 \mu s$

Figure 12: Bubble evolution with time

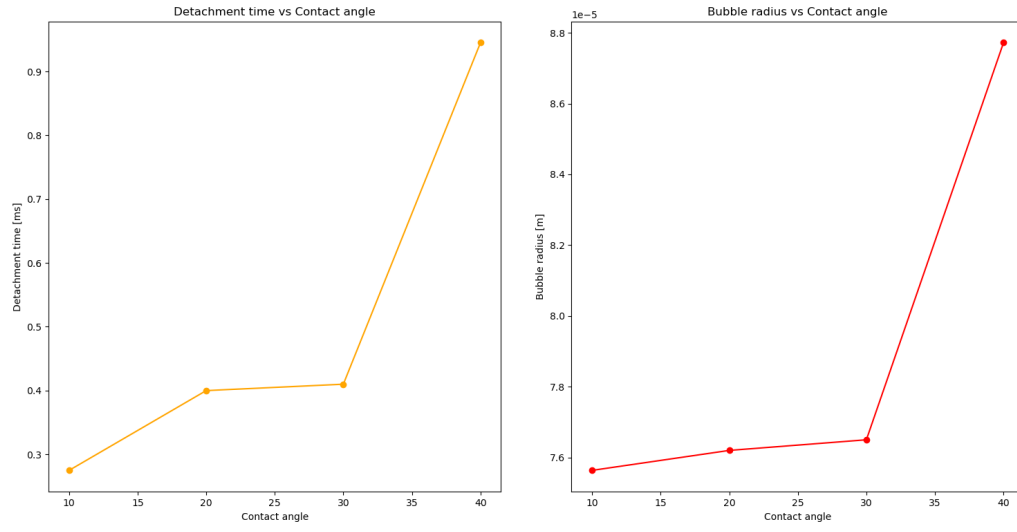


Figure 13: Impact of the contact angle on bubble detachment radius and time.

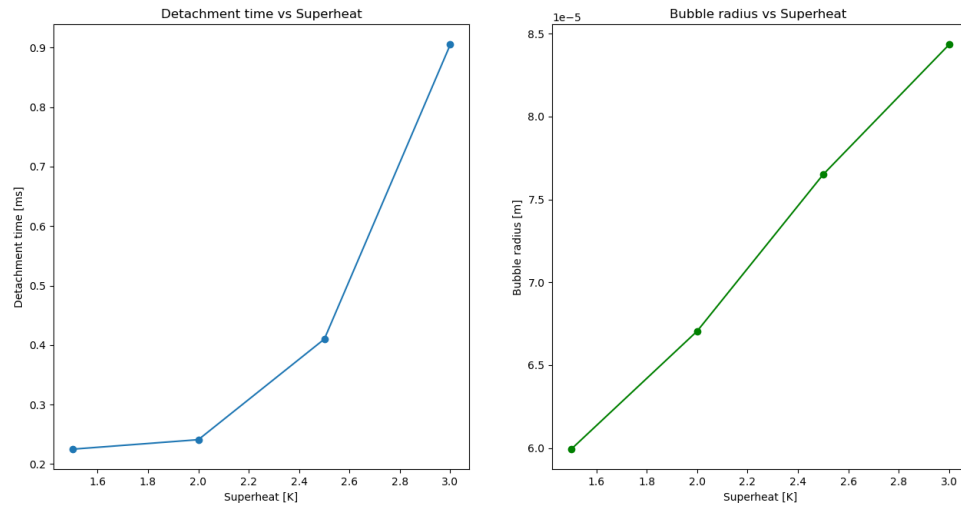


Figure 14: Impact of the superheat on bubble detachment radius and time.

References

- [1] Fmuni. GitHub - fmuni/boilingFoam-PUBLIC: OpenFOAM-based solvers, libraries, and test cases for simulating boiling flows.
- [2] F. Municchi, C.N. Markides, O.K. Matar, and M. Magnini. Computational study of bubble, thin-film dynamics and heat transfer during flow boiling in non-circular microchannels. *Applied Thermal Engineering*, 238:122039, 11 2023.
- [3] Anastasios Georgoulas, Manolia Andredaki, and Marco Marengo. An Enhanced VOF Method Coupled with Heat Transfer and Phase Change to Characterise Bubble Detachment in Saturated Pool Boiling. *Energies*, 10(3):272, 2 2017.
- [4] Gangtao Liang and Issam Mudawar. Pool boiling critical heat flux (chf) – part 1: Review of mechanisms, models, and correlations. *International Journal of Heat and Mass Transfer*, 117:1352–1367, 2018.
- [5] Christian Mulbah, Can Kang, Ning Mao, Wei Zhang, Ali Raza Shaikh, and Shuang Teng. A review of vof methods for simulating bubble dynamics. *Progress in Nuclear Energy*, 153:104478, 2023.
- [6] J.U Brackbill, D.B Kothe, and C Zemach. A continuum method for modeling surface tension. *Journal of Computational Physics*, 100(2):335–354, 6 1992.
- [7] S. Hardt and F. Wondra. Evaporation model for interfacial flows based on a continuum-field representation of the source terms. *Journal of Computational Physics*, 227(11):5871–5895, 3 2008.
- [8] L.E. Scriven. On the dynamics of phase growth. *Chemical Engineering Science*, 10(1):1–13, 1959.